JOURNAL OF PROPULSION AND POWER
Vol. 18, No. 3, May–June 2002

Burning Aluminum Particles Inside a Laboratory-Scale Solid Rocket Motor

John C. Melcher,* Herman Krier,† and Rodney L. Burton‡
University of Illinois at Urbana–Champaign, Urbana, Illinois 61801

Single and agglomerated aluminum droplets were studied in a solid rocket motor test chamber with optical access to the internal flow at 6–22 atm and 2300 K. The chamber was pressurized by burning a main grain ammonium perchlorate/hydroxyl-terminated poly-butadiene propellant, and the burning aluminum droplets were generated by a smaller aluminized solid propellant sample, center mounted in the flow. A 35-mm camera was used with a chopper wheel to give droplet flame diameter vs time measurements of the burning droplets in flight, from which burning rate laws were developed. A high-speed video charge-coupled device with high-magnification optics imaged the flame/smoke cloud surrounding the burning liquid droplets. The intensity profiles of the droplet images were deconvoluted using an Abel inversion to give true intensity profiles. Both single and agglomerated droplets were studied, where agglomerates comprise hundreds of parent particles or more. The Abel inversions show that the relative smoke cloud size is not constant with diameter, but instead grows as the droplet shrinks, by $\sim D^{-0.5}$, for both the single and agglomerated droplets. Measured diameter trajectories show that, for single droplets, the mean diameter law is $D^{0.75} = D_0^{0.75} - 8 \cdot t$, and, for agglomerated droplets, $D^{1.0} = D_0^{1.0} - 20 \cdot t$. For both single and agglomerated droplets, the burning rate slope k did not change significantly for the chamber pressure range studied.

Nomenclature

a	=	prefactor constant for $D_{\text{image}}(t_b - t)$ curve fit
b	=	diameter power for $D_{\text{image}}(t_b - t)$ curve fit
D	=	diameter, μm
D_{image}	=	burning droplet image diameter, μm
D_{surf}	=	aluminum droplet surface diameter, μm
D_0	=	initial aluminum droplet diameter, μm
k	=	burning-rate constant, μm^n/ms
n	=	burning-rate diameter power
p	=	pressure, atm
R_k	=	Hermsen relation correction factor
r/r_s	=	nondimensional smoke cloud size
r_s, r_{surf}	=	droplet surface radius, μm
T	=	temperature, K
t	=	time, ms
t_b	=	droplet burning time, ms
X_{eff}	=	effective oxidizer mole fraction
x	=	arbitrary variable
y	=	arbitrary variable
α	=	prefactor coefficient for $r/r_s(D_{\text{surf}})$ curve fit
β	=	diameter power for $r/r_s(D_{\text{surf}})$ curve fit
Γ_1, Γ_2	=	gamma-distribution shape parameters

Introduction

A DETAILED review of aluminum combustion was presented in Refs. 1 and 2, and a condensed version is presented here. Aluminum particles have a characteristic oxide coating that must be melted or cracked open before the aluminum particle can ignite. Because the oxide melting temperature, 2327 K, is higher than the melting temperature of aluminum, 933 K, the aluminum is fully melted on ignition. Furthermore, the aluminum and aluminum oxide are insoluble,[3] and the initial oxide coating coalesces into a cap on the molten aluminum droplet surface. The droplet surface burns at a temperature between the oxide melting temperature, ~2300 and ~2700 K, the aluminum boiling temperature at 1 atm. Although the global oxidation reaction of aluminum produces alumina, Al_2O_3, many suboxides such as AlO, AlO_2, Al_2O, and Al_2O_2 exist in the flame zone, with AlO as the most prominent.

Aluminum combustion is often studied in air, where it is found that aluminum droplets burn in a gas-phase reaction where the flame front is at a detached distance away from the droplet surface. The condensation of alumina at ~3800 K in a 300-K, 1-atm air environment limits temperature of the flame/Al_2O_3 oxide cloud. For $\mathcal{O}$(100-μm) droplets burning in 1-atm air, the mechanism is considered diffusion controlled because the species are reacting much faster than the diffusion rates at the elevated temperatures.

In a solid rocket motor, pressures and temperatures are elevated and O_2 (g) constitutes less than 1% of the equilibrium combustion products. However, because of the polymer/oxidizer composition of solid propellants, H_2O (g) and CO_2 (g) are abundant. For example, in our experiments using an ammonium perchlorate/hydroxyl-terminated poly–butadiene (AP/HTPB) propellant, the major propellant combustion products are calculated to consist of 41% H_2O (g), 12% CO_2 (g), 18% HCl (g), and only 0.8% O_2 (g), by mole fraction. A detailed description of the kinetic rates for Al burning in H_2O and CO_2 is presented in Ref. 4. Furthermore, it has been shown that under these conditions, the droplet flame may no longer be diffusion controlled as in 1-atm air conditions, but instead shifts to a distributed, reaction-rate limited mechanism, as hypothesized in Fig. 1.[1,4]

The combustion of aluminum droplets can be characterized by the droplet burning time, which has been shown to depend on state properties of the environment and the flow characteristics of the entrained droplet. Classical fuel droplet combustion theory states the diameter of a burning droplet as $D^2 = D_0^2 - k \cdot t$. The burning time can be defined as $t_b \equiv D_0^2/k$. The state properties of the medium, most important gas temperature and oxidizer concentrations, affect the burning rate coefficient k. An increase in burning rate results in a shorter burning time for a given droplet size.

Research has shown that the diameter dependence does not necessarily follow the classical D^2 law, but instead follows D^n, where

Received 20 June 2001; revision received 9 January 2002; accepted for publication 22 January 2002.

*Ph.D. Candidate, Department of Mechanical and Industrial Engineering. Student Member AIAA.
†Professor, Department of Mechanical and Industrial Engineering. Fellow AIAA.
‡Professor, Department of Aeronautical and Astronautical Engineering. Associate Fellow AIAA.

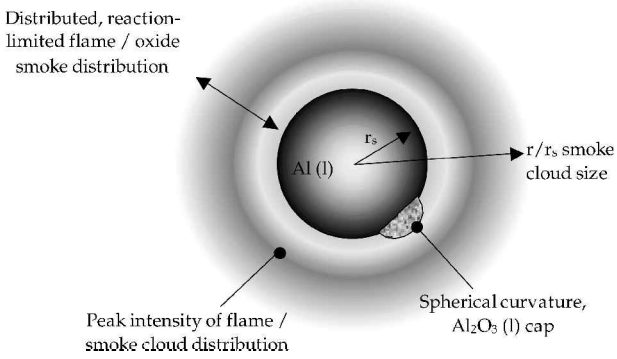

Fig. 1 Schematic of aluminum droplet combustion in SRM conditions.

n is typically between 1.5 and 2. Work presented in Ref. 1 showed that the droplet burning rate in typical solid rocket motor (SRM) conditions was much greater than the burning rate of droplets in 1-atm, 300-K air. The burning time for aluminum droplets at 10–20 atm and 2300-K conditions was measured to be $t_b = D_0^n/280$, where $n = 1.65 \pm 0.55$. This rate is a factor of seven times faster than those found at 1-atm, 300-K air combustion.[5]

A commonly used empirical model for aluminum droplet burning time in SRM conditions is the Hermsen model,[6] Eq. (1), which was developed by comparing measured to predicted specific impulse and then adjusting aluminum combustion efficiency parameters. The empirical exponents on the diameter, pressure, and gas composition were based on the experimental work of Davis,[7] Pokhil et al.,[8] and Hartman,[9] respectively. The Hermsen correlation[6] is given in Eq. (1), and serves as a basis of comparison for the results presented in this paper:

$$D^{1.8} = D_0^{1.8} - kt$$

$$k = 8.3314 \times 10^{-5} \cdot R_k \cdot X_{\text{eff}}^{0.9} \cdot p^{0.27} \ (\text{cm}^{1.8}/\text{s})$$

$$X_{\text{eff}} = \left(X_{O_2} + X_{H_2O} + X_{CO_2} + X_{OH} + X_O\right)^* 100\%$$

$$R_k = 1 (\text{laboratory scale}) \text{ or } 2.7 (\text{operational SRM}) \qquad (1)$$

A key objective of this research is to characterize the burning rate and flame structure of aluminum droplets using optical imaging through a windowed solid propellant rocket test chamber. Chamber conditions are generated using an AP/HTTB solid propellant operating at pressures up to 25 atm; the aluminum source is a smaller aluminized propellant sample. Both single and agglomerated droplets are studied, and the sizes of the aluminum particles loaded in the aluminized sample were on the order of magnitude of 10–100 μm. Data were recorded using a 35-mm camera/chopper wheel setup, as well as high-magnification optics mounted to a high-speed charge-coupled device (CCD) video camera. Emphasis was placed on the agglomerated aluminum droplets' burning time, flame/smoke structure, and propellant surface formation processes. The quantified effect of the parameters is used to compare with and validate other models for burning rate.

Furthermore, we investigated agglomeration phenomena that may alter the aluminum combustion in SRM conditions. When high-speed CCD video and high-magnification optics are used, it is possible to image the agglomerating propellant surface burning and in-flight agglomerate events, such as agglomerate explosions, jetting, and fragmentations.

The work presented here builds on previous work presented in Ref. 1. The major experimental addition to the research in this paper was the use of the high-speed CCD video camera and Abel inversion analysis, as well as the study of agglomerating propellants.

Experimental Techniques

Apparatus

Laboratory-Scale SRM

This experiment studies aluminum droplets in situ, within the rocket motor chamber with hot solid propellant gaseous combustion products. The aluminum droplet source is an aluminized solid propellant, which is used in small amounts to avoid overexposing the cameras with intense radiation from the burning aluminum droplet field. The experiment utilizes a chamber with 30-cm-long axial observation windows for axis to the continuous flow that lasts 2–3 s; details may be found in Ref. 2. Figure 2 shows the overall experiment schematic. The chamber allows for a vertical flow traveling upward from a source propellant in the bottom of the chamber to a discharge through a choked-orifice nozzle at the top. The small aluminized propellant sample is mounted on a pedestal in the center of the square channel, in the bottom half of the window view.

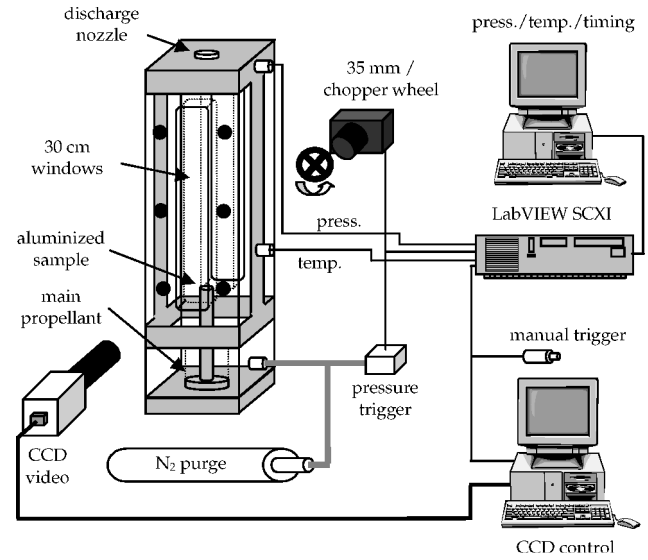

Fig. 2 Experiment layout schematic: larger main propellant serves to pressurize and heat the chamber, and the smaller aluminized sample serves as the aluminum droplet source.

Two propellant samples burn simultaneously during each experiment: a relatively large (22-g) nonaluminized bimodal propellant to fill the chamber to test conditions and a much smaller (~0.1 g) aluminized propellant sample to inject aluminum droplets. The main composite propellant is a mixture of 88% bimodal AP oxidizer and 12% fuel binder by weight, hand mixed in the lab. The oxidizer is a composite of two sizes of AP: 62% 200-μm AP, and 38% 50-μm AP. The fuel binder is a mixture of 77.4% HTPB fuel, 5.9% dioctyl adipate (DOA) plasticizer, and 16.7% isopherone diisocyanate (IPDI) curing agent. The propellant is ignited by applying a 5-A current across a nichrome wire sandwiched between the top of the main propellant and another wafer of propellant of mass ~3 g. The aluminized propellant sample is ignited by the hot gases from the main propellant shortly after the ignition spike and burns throughout the remainder of the main propellant pressure trace.

Both pressure and temperature were measured in the center square channel where aluminum combustion occurs. Because the experiment lasts for only a few seconds, a fast thermocouple response time was required. An Omega open-sheath, type C (tungsten–rhenium, rated up to 3000 K) thermocouple with 0.23-mm bead was used. It was calculated to have a 125-ms response time at chamber flow conditions. A typical measurement of pressure and temperature is presented in Fig. 3. A linearly rising pressure trace was observed in each experiment, with nearly identical slope. This ramp in the pressure is useful because it creates a variable pressure condition for our studies. As further described in Ref. 1, a quasi-steady chamber model was developed to investigate the cause of the pressure ramp, and a heat transfer model with a chamber wall temperature that increased linearly in time was found to match the data. Accounting for radiation losses from the thermocouple bead, the measured temperature of ~2200 K is corrected to ~2300 K. It was also found that the temperature did not change significantly with pressure, and the temperature was assumed constant in the study.

By the use of a 35-mm open shutter camera and chopper wheel, the typical droplet velocity was measured to be 5–7 m/s, which

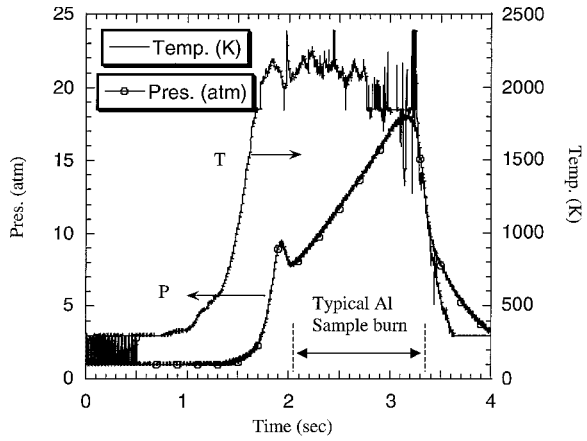

Fig. 3 Typical experiment test conditions, pressure, and thermocouple temperature measurements.

agrees well with a calculated mass-averaged gas velocity of 5.1 m/s across the channel area. The burning droplet images often exhibited convective trails, indicating a slight droplet slip velocity.

Because of the elevated pressure and temperature, and low flow velocity inside the chamber, one can assume that the product species shift over a short distance to equilibrium, providing a near-constant composition in the upper part of the chamber where the aluminum droplets burn. Equilibrium gas composition for the experiment was calculated using the TEP code and defining the propellant composition by mass fraction and specified chamber pressure.[10] At 13-atm (the baseline pressure for the single droplet burn-time study), the adiabatic flame temperature is ~2900 K and the gas composition is 41% H_2O, 18% HCl, 12% CO_2, 10% N_2, 9% CO, 4% H_2, 2% OH, 2% Cl, and only 0.8% O_2, by mole fraction. The solid propellant mixture yields very little excess oxygen, but ample water vapor and carbon dioxide are available for aluminum combustion. Because the key combustion products are stable molecules (H_2O, HCl, CO_2, and N_2), we assume negligible recombination or dissociation as the flow cools away from adiabatic to the measured temperature of ~2300 K.

Cameras and Optics

A 35-mm camera with an optical chopper wheel is used in open shutter operation to obtain data on the aluminum droplets' burning diameter time history. A high-speed CCD video camera is used to freeze in-flight large-magnification images of the burning droplets and to record video sequences of the burning propellant surface. As shown in Fig. 2, the chamber's dual-window design allows both instruments to be used simultaneously during a single experiment.

The 35-mm camera used for data photography in the droplet burning-rate experiments is a Canon Eos Rebel G, with a 50-mm, 1:1.8 Canon lens. For all such experiments, the shutter speed is set at either 1/30 or 1/20 s, and the largest aperture opening, ƒ/1.8. The timing of the 35-mm camera operation is set by the chamber pressure, as shown in the schematic in Fig. 2.

An optical chopper wheel was used to give time resolution to the recorded burning droplets. A Thorlabs, Inc., Model MC100 variable frequency optical chopper was mounted in front of the lens and set at a chopping frequency of 1000 Hz. Optical chopping gives the droplet trajectory a dashed appearance, so that individual droplet images can be resolved in time to give image diameter vs time measurements. The photographs are digitized using a Nikon Super CoolScan 2000, which scans directly from the photograph negative at 2700 dpi, 8-bit per color (red–green–blue). Typical experiment results and analysis for the 35-mm camera/chopper wheel are presented in detail in Refs. 1 and 2.

A high-speed CCD video camera was used to study the burning droplets under high magnification. The high-speed video was used for several reasons. First, a fast shutter time was required to freeze-frame the burning droplets. Second, because the depth of focus is so limited under high magnification, a continuous video camera was used to obtain as many in-focus image frames as possible. The camera is a Redlake Imaging MotionScope 8000S model, with an 8-bit monochrome CCD array. At the normal operating frames per second rate used in this study, 2000 frames/s the array is 160 × 140 pixels in size and can record data for 2 s. As shown in Fig. 2, a timing mark is concurrently sent to the data acquisition system, so that the image frames can be referenced to their corresponding pressures.

To obtain high magnification, the high-speed CCD video camera is affixed with a 75-mm C-mount lens with Hoya UV and Vivitar +4 close-up ring adapters. The aperture was typically set at ƒ/5.6 as the optimal opening for exposure control and focus depth, and, with these settings, the camera was typically mounted ~22 cm from the center of the combustion channel. The shutter speed of the camera was nominally 1/30,000 s, or 33 μs, operating at 2000 frames/s. For the flame/oxide cloud size study of the burning droplets, the CCD video camera was focused about 60 mm above the aluminized sample surface, with a field of view 3.6 × 3.2 mm.

Data Reduction, Abel Inversion Analysis

The images of the burning droplets are analyzed by applying a user-written MATLAB® routine, which incorporated several of the functions in the MATLAB Image Processing Toolbox. The purpose of the code is to measure true radial intensity slices through the droplets and surrounding flames, then deconvolute these intensity profiles using an Abel inversion to obtain a true radial intensity profile. Details of the Abel inversion analysis are presented in Ref. 2.

Because the recorded burning droplet images are two-dimensional integrated, line-of-sight projections of three-dimensional events, the intensity profile was deconvoluted to obtain the actual radial intensity profile. The Abel inversion works on a cylindrically symmetric radial profile. If the burning droplets were spherically symmetric, any planar slice along the droplet axes would be cylindrically symmetric. However, due to the convective environment in this experiment, the droplets often burn with a convective tail, rendering the upper portions of some droplet images not spherically symmetric. Therefore, intensity data were only analyzed on a single line passing through the droplet center and perpendicular to the slip velocity vector (as discussed hereafter), ensuring spherical symmetry.

The 8-bit, black-and-white experiment images were enlarged by a factor of 4 times using the bicubic interpolation of the imresize function in MATLAB. Magnification of the image increased the number of data points along a given radial intensity slice, therefore reducing the signal noise in the Abel inversion calculation. Raw intensity profiles are measured using the improfile MATLAB function across a user-defined line that passed the center of the burning droplet image. Figure 4 shows the enlarged droplet image and intensity profile line and the raw intensity data.

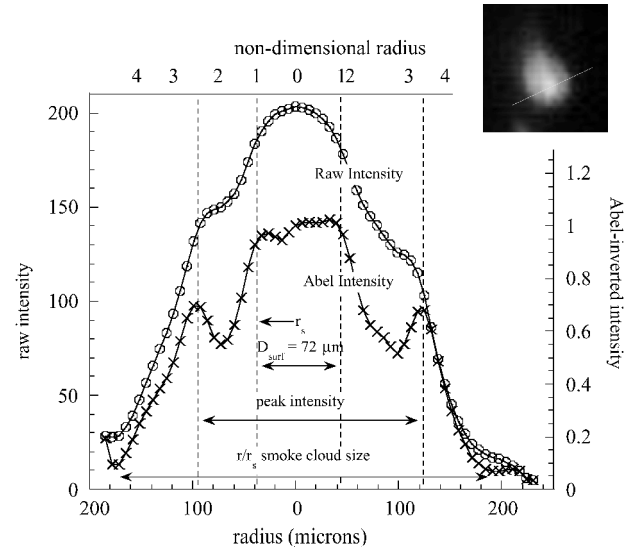

Fig. 4 Example of data reduction process for a single droplet, 72-μm diameter, burning at 7.3 atm: high-speed CCD video frame, digitally magnified 4 times with intensity profiling line on droplet, and resulting raw and Abel-inverted intensity profiles.

To perform the Abel inversion on the raw intensity data, Dasch's recommended three-point method for Abel inversion was incorporated into the MATLAB routine.[11] Dasch's paper contains an error, and his relation [Eq. (7) of Ref. 11] was later corrected by Hanson-Parr of the Naval Air Warfare Center, China Lake, California, in a personal communication in February 2000. For the Abel inversion calculation, the raw intensity profile was divided into two halves at the droplet center, and the code operated on the two halves separately. The resulting deconvoluted image intensity profile is shown in Fig. 4.

The droplet image intensity data were analyzed to obtain the size and characteristics of the smoke/flame region. The droplet surface was defined by examining the burning droplet image, raw intensity profile, and Abel-inverted intensity profile. The droplet surface is first measured to establish a basis for a nondimensional radius, which is calculated on the two halves separately. The Abel data are then used to measure the nondimensional radial location of the peak in the intensity, as well as the overall size of the smoke cloud surrounding the droplet. In the example droplet in Fig. 4, the droplet is measured to be 72 μm at that instant. The peak intensity is located at $(r_{\text{peak}}/r_s) = 2.5$ radii on the left side of the droplet and 3.6 on the right (average: 3.1). The overall size of the smoke/flame cloud is 4.5 radii on the left and 5.5 on the right (average: 5.1).

Aluminized Propellants Studied

A small, aluminized propellant sample of size approximately $3 \times 3 \times 8$ mm^3 and mass $\sim$0.1 g was mounted on a pedestal in the center of the square channel in an end-burning configuration. Two different types of burning aluminum droplets, singles and agglomerates, were studied. To study these two types of burning droplets, two different aluminized propellant test samples were used.

Nonagglomerating Propellant

The nonagglomerating propellant studied was manufactured by Thiokol Corporation and is designated Thiokol 1, which is an AP/HTPB bimodal propellant, similar to the base propellant used to pressurize the chamber. Scanning electron microscope (SEM) images of the burning propellant are presented in Ref. 1. The aluminum loaded is 15% of the propellant mass. A size analysis of the aluminum particles visible in the propellant SEM shows an average size of 106 ± 20 μm.

To predict the likelihood of particle agglomeration, the aluminum behavior near the burning propellant surface must be considered. At the chamber operating pressure, the thermal heat-up layer near the propellant surface is only $\sim$15 μm. The propellant falls under the large particle regime in the Gany and Caveny model[12] and, accordingly, shows little if any agglomeration. For this propellant sample, agglomeration was not observed in 1-atm tests, where agglomeration would be most likely to occur. Therefore, it is assumed that the propellant does not agglomerate under SRM test conditions either.

Agglomerating Propellant

The agglomerating propellant used here at University of Illinois at Urbana–Champaign (UIUC) was manufactured by Alliant Techsystems, Inc., and is designated as Alliant 1. Like the other propellants described, the Alliant 1 propellant is a bimodal, AP/HTPB propellant with additional ammonium nitrate (AN) oxidizer, and is 20% 15-μm aluminum by weight. There is a significant size difference between the large-mode AP and the Al particles, which have ample pocket volume between the 200-μm AP particles to collect for agglomeration. At a chamber operating pressure of 15 atm, the Alliant 1 propellant is calculated to have a $\sim$13-μm thick thermal heat-up layer, which is the same order of magnitude as the aluminum size, thus leading to agglomeration.

Surface Agglomeration Video

The high-speed CCD video camera was used with a reverse-mounted, 20-mm Nikon F-mount lens to image combustion phenomena at and near the aluminized propellant surface at both 1 atm and pressures exceeding 10 atm. Under these conditions, the camera typically was set at f/11 with a framing rate of 250 frames/s (480×420 pixel array) and a 1/250-s shutter. Because of the intense magnification, one or two 250-W spot lamps were often employed for lighting.

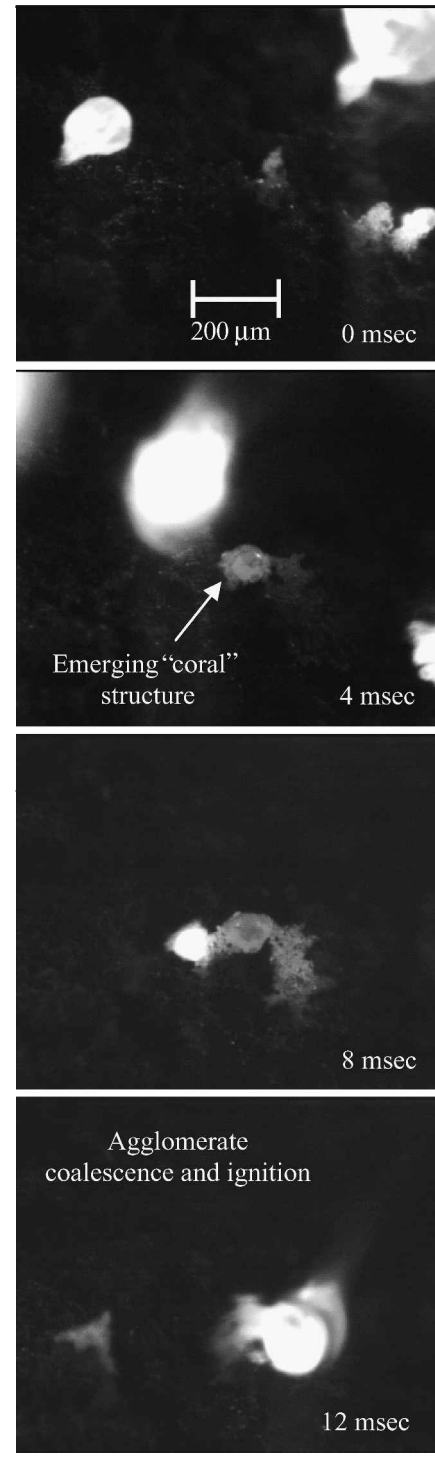

Fig. 5 High-speed CCD video of Alliant 1 agglomerating propellant burning at 1-atm pressure (in room temperature air); image frames 4 ms apart and ~ 1 mm wide.

At 1-atm (air) conditions, an agglomerate is formed by corallike clusters of aluminum that are exposed at the surface near the same time and is then entrained in the flow shown in Fig. 5. Other agglomerates are observed to stick to the surface, moving around and absorbing more aluminum. Although quench tests were not performed on the propellant surface, it is assumed that the corallike cluster is initially a buried vein or pocket of loaded aluminum that sinters together and exposes as a single structure before agglomeration as the

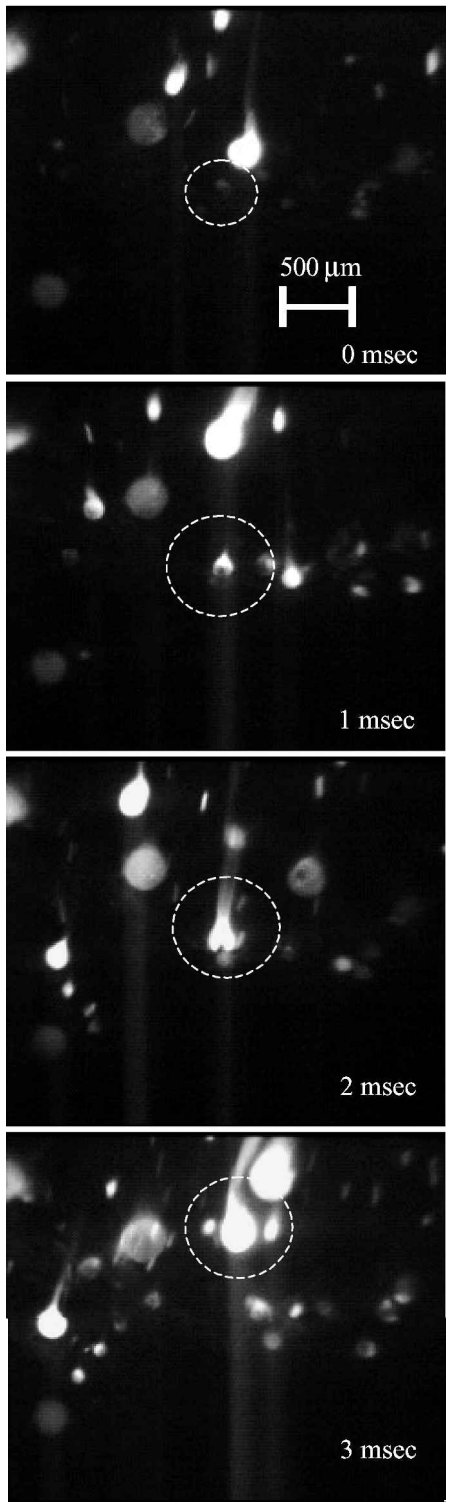

Fig. 6 High-speed CCD video frames of Alliant 1 burning surface in 13.4-atm, SRM experiment conditions.

propellant surface regresses. The coral-forming mechanism is the primary agglomeration process at 1 atm for this propellant. This observation is contrary to the straight pocket model of agglomeration, which does not predict such coral structures.[3]

Further studies were conducted of the Alliant 1 agglomerating propellant at SRM chamber conditions. As shown in Fig. 6, no coral structures, as observed at 1 atm, are observed in the SRM conditions at 13.4 atm. Thus, we presume that the pocket model of agglomeration dominates the agglomeration process in the SRM condition. The primary difference between the two conditions is the pressure and the resulting propellant burning rate. With the decreased thermal melt layer under high pressure, the parent aluminum particles do not have the time to sinter into the large coral structures, and only smaller pockets of aluminum will have such time to sinter and agglomerate. We calculate the thermal layer for the propellant at 1 atm (Fig. 5) is ~36 μm, and ~14 μm at 13.4 atm (Fig. 6).

At chamber conditions, a wide range of agglomerate sizes were observed leaving the propellant surface, some as small as ~35 μm in diameter and others larger than 500 μm in size. Most agglomerates left the surface in the size range of 120–200 μm diameter. Although the agglomerates formed in the SRM flow were generally smaller than those formed in 1-atm air, there was no discernable relationship between agglomerate size and pressure over the range studied.

Agglomerate Fragmentation

Another key observation in the propellant surface video is that some agglomerates are generated with large oxide caps that greatly disrupt the droplet flame symmetry during the first few milliseconds of motion away from the propellant surface. These caps are the residual oxide mass from the initial oxide shells encompassing the parent particles. At SRM conditions, the initial flame asymmetry is observed in 20–30% of the agglomerates. For affected agglomerates, smoke cloud symmetry is usually gained within the first 5–10% of the droplet burn time, either spherically or cylindrically symmetric (axis parallel to local flow), depending on the presence of a convective tail.

Although it is possible that the flame is simply spreading itself symmetrically, even over the initial cap, another likely explanation exists. It may be possible that the agglomerate rejects the initial oxide cap mass. Recall that the oxide cap and the aluminum are insoluble.[3] Under the convective tail, the initial cap may be separated from the agglomerate as a single large ejection or a stream of smaller ejections, both of which are observed to occur. This hypothesis is supported by results reported by Brulard, who photographed agglomerates spitting off several particles from the convective tail when burning in 1-atm air.[13] It is apparent from the images that the region downstream of the droplet is laminar, both in 1-atm and SRM flow conditions, and one could assume that the separation would not be due to the strength of the wake downstream of the droplet. Another possible explanation lies in the chemical interactions involved at the aluminum droplet surface under the oxide cap that could potentially lead to oxide cap ejection. A sample video image sequence is shown in Fig. 7 for an agglomerate burning during its first few milliseconds of its burn time in 1-atm, room-temperature air conditions near the propellant surface. The aluminized propellant sample was ignited from room temperature conditions. Because the droplet is only ~5 mm above the burning propellant sample surface, the local environment temperature and gas composition will be very near to SRM conditions (albeit at 1 atm). The burning agglomerate is clearly seen ejecting liquid-phase oxide particulates from the top of the oxide cloud. The ejected particulates are assumed to be oxide because their radiative intensity matches the oxide cap intensity. Note that although the oxide cap on the droplet surface appears to move around on the surface, one cannot tell the difference between the cap rotating or the droplet rotating.

Similar ejections were observed in the test motor conditions, but were not as easy to detect against the bright SRM flow background. In Fig. 8, particulate ejections can be seen in the convective tail of a ~290-μm agglomerate burning at 8.6-atm SRM experiment conditions within the first few milliseconds of its burn time. These results indicate that oxide cap ejection can contribute to retaining flame/smoke cloud symmetry around the burning agglomerates, even in the SRM experiment conditions. An alternative interpretation is that the particulate ejection results from fine oxide smoke coagulation in the cloud, hinted at the location of the ejection in Fig. 7. However, the ejection phenomenon is primarily observed only in the initial stages of droplet combustion, which eliminates a fine smoke coagulation mechanism acting alone.

Agglomerated droplets may have a heterogeneous composition due to contaminant entrainment during formation on the propellant surface, and such agglomerates may exhibit spinning, jetting, fragmentation, or explosions. The high-speed CCD video camera was

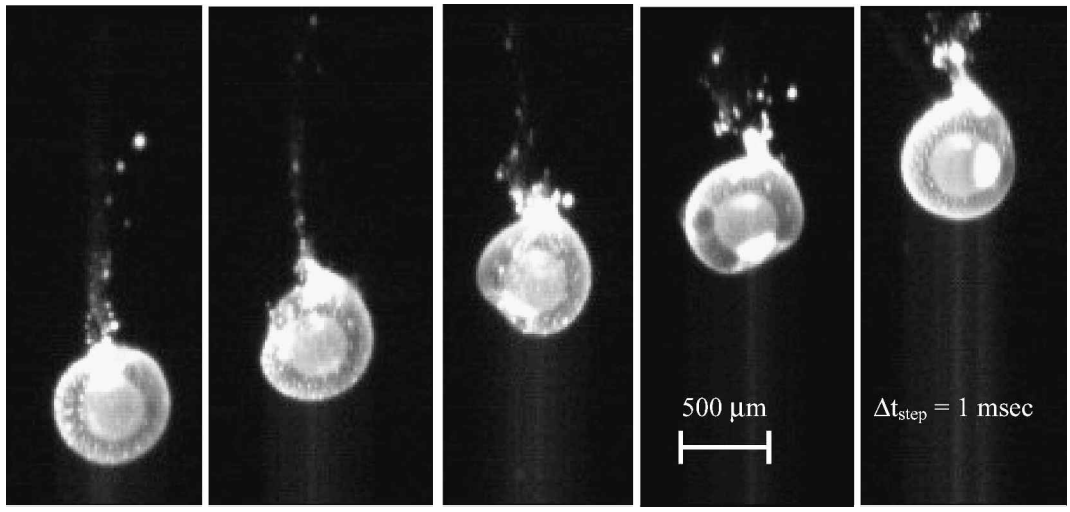

Fig. 7 Sequence of particulate ejection from ~ 380-μm agglomerate burning in 1-atm; frames 1 ms apart and ~ 5 mm above Alliant 1 propellant sample surface.

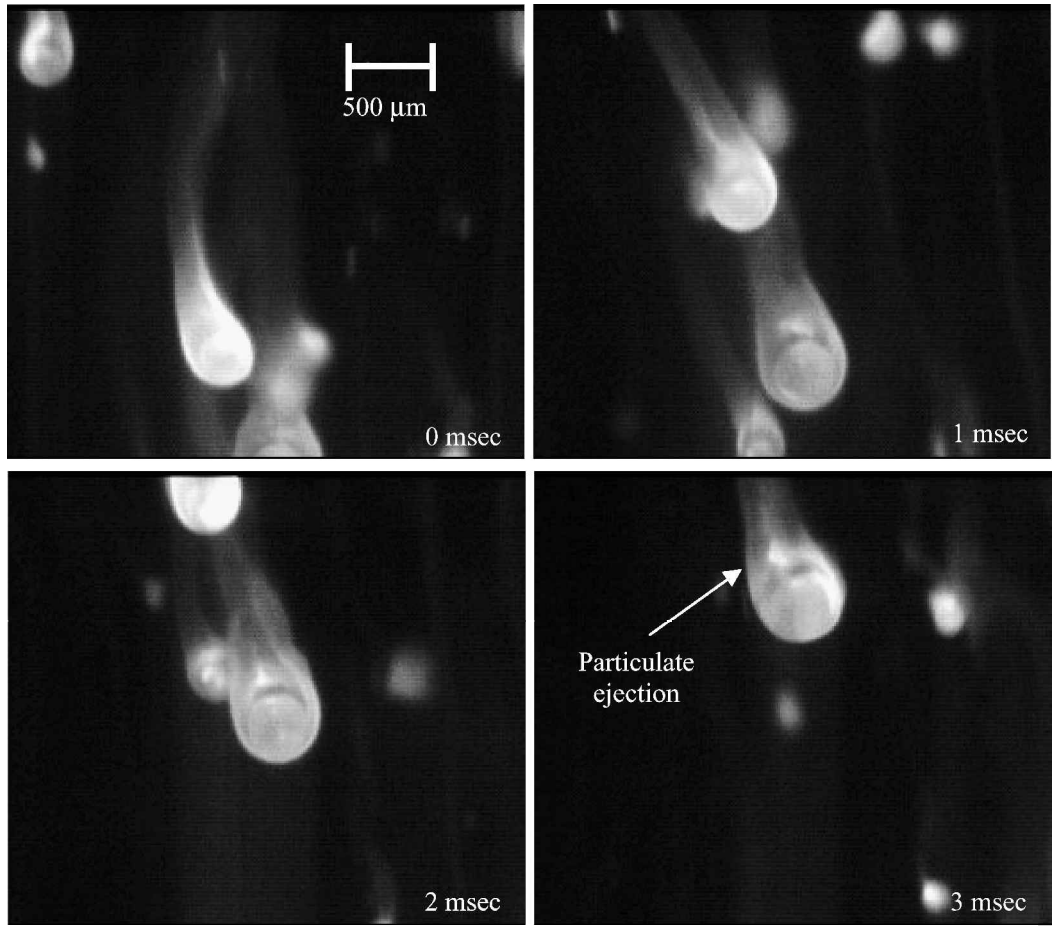

Fig. 8 Sequence of particulate ejection from ~ 290-μm agglomerate burning in 8.6-atm SRM experiment conditions; frames 1 ms apart and ~ 5 mm above Alliant 1 propellant sample surface.

used in a study to determine the percentage of agglomerates that explode or fragment instead of burning out in a continuous manner. A large field of view was used so that the number of particles entering the frame, as well as the number of agglomerates exploding, could be counted. When burning in 1-atm air, ~15–20% of agglomerates did explode, and the agglomerate explosions are very brilliant. An explosion is characterized by sudden and complete particle annihilation in contrast to the oxide particulate ejection shown in Fig. 7. The agglomerates exploded at various times during their burn history, but were chiefly observed in the latter half of the typical droplet lifetimes. Details of this experiment are presented in Ref. 2.

Similar large-field CCD recordings were made of the agglomerates burning in chamber experimental conditions over 6–21 atm pressure, and no droplet explosions were ever observed. Thus, the agglomerate explosion phenomena has virtually no effect on the

agglomerate burn-time model for SRM conditions developed in this study. Likewise, single, nonagglomerated droplets would have relatively low heterogeneity and did not exhibit any spinning, jetting, or explosions in laboratory experiments, both in 1-atm air and SRM conditions.

Micheli and Schmidt claim that particle fragmentation would be an insignificant effect in SRM conditions due to a lack of O_2 (Ref. 14). However, it is more likely that the lack of explosions in SRM conditions compared to the typical explosions in 1-atm air stems from the differences in agglomerate formation processes, as described in the preceding section. Recall that the agglomerates seem to form by exposed corallike structures in 1-atm air, but are formed by the pocket model in the SRM conditions. If the coral-exposing process inherently forms structurally less stable agglomerates than the pocket model, then those agglomerates in 1-atm air would be more likely to fragment. The coral-formed agglomerates may be less uniform in composition, with more initial oxide shell material from the parent particles distributed throughout the agglomerate. This is supported by SEM imaging of agglomerates by Price and Sigman, who show whole oxide shells enclosed within the formed agglomerates.[3] This hypothesis would indicate that the agglomerates formed in SRM conditions by the pocket model are more uniform and closed, perhaps with the initial oxide shells formed neatly into the initial oxide cap, more similar to a single (nonagglomerated) droplet.

Results and Discussion

The data for the flame/smoke cloud size presented hereafter have a common characteristic of broad scatter. This scatter is not due necessarily to the data reduction method because, if this were the case, the scatter range would increase at smaller wavelengths, which was not observed. Instead, the scatter is from the inherent stochastic nature of the aluminum combustion events in SRM conditions. For example, if the oxide cap on the molten droplet surface varies just slightly in size from droplet to droplet, then the overall smoke cloud size and burning rates would vary as well. In the case of agglomerates, the composition quality of the molten droplet can vary droplet to droplet, affecting both the smoke cloud size and burning rate.

Although the percentage of surface area coverage by the oxide cap greatly influences the droplet burn rates, the percentage would have little effect on the droplet diameter measurement. The aluminum droplet retains a spherical shape whose diameter is defined by the aluminum mass. Therefore, the size of the oxide cap or the subsequent surface area coverage is not addressed in the droplet diameter analysis.

Abel Inversion Data

To verify further that the droplets were imaged with smoke clouds dominated by thermal emission from the hot oxide smoke, two data sets are presented at two wavelengths, 490 nm, where AlO emits strongly, and 560 nm, where no AlO emission occurs. As described in Refs. 1 and 2, the two wavelengths were studied using ±9-nm bandpass filters combined with a neutral density filter to match the change in thermal emission. As will be shown, the data at the two wavelengths lie close together within the scatter. Hence, the flame/smoke cloud regions in the images are dominated by thermal emission from the hot oxide particles, and not AlO chemiluminescence, which agrees with work by Brewster and Taylor.[15]

Single Droplets

The smoke cloud size is nondimensionalized by the surface diameter D_{surf}, and each r/r_s data point (out of the 325 shown) represents the average of two halves of one droplet image. The data presented in Fig. 9 are for single, nonagglomerating droplets burning in SRM flow conditions, $p = 1$ and 6.7–20.1 atm. The plot shows 325 data points and each point represents the average of two halves of one droplet image. The combined 490- and 560-nm data are curve fit as $r/r_s = \alpha \cdot D_{\text{surf}}^{-\beta}$, where we obtain $\alpha = 53 \pm 18$ and $\beta = 0.55 \pm 0.10$, represented by the mean (solid) line and the error (dashed) lines

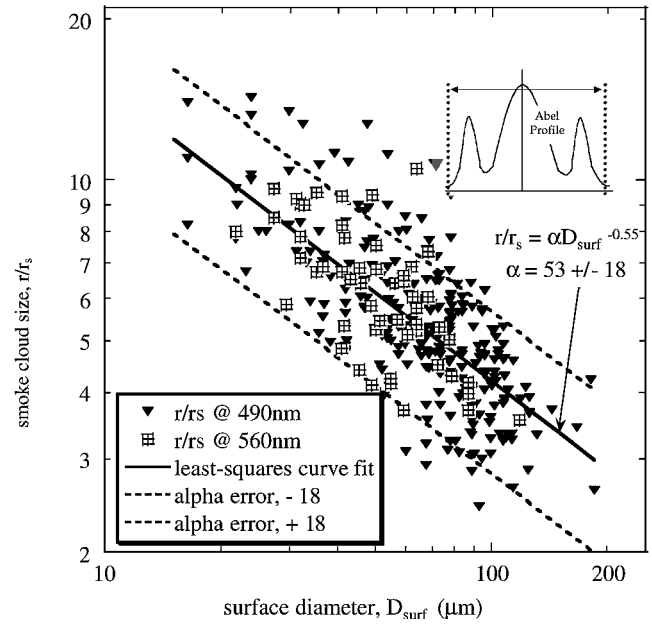

Fig. 9 Nondimensional size of oxide cloud surrounding burning droplet vs droplet diameter for single droplets burning in SRM flow conditions, $p = 1$ and 6.7–20.1 atm; combined 490- and 560-nm data (325 points) are curve fit as $r/r_s = \alpha \cdot D_{\text{surf}}^{-\beta}$, where $\alpha = 53 \pm 18$ and $\beta = 0.55 \pm 0.10$.

in Fig. 9. That is, as the droplet diameter gets smaller, the smoke cloud's relative size grows.

The growing relative size of the oxide cloud with shrinking diameter can be potentially explained by considering that the oxide cap grows on the droplet surface as the droplet burns. As the droplet gets smaller, the oxide cap covers a larger percentage of the droplet surface area. The oxide cap can reduce the percentage of free aluminum surface area to only 20–40% of the droplet surface area for single droplets. One may presume then that as less pure aluminum surface area is available as the droplet gets smaller, the droplet flame becomes fuel-lean in a reaction-limited regime. Under these fuel-lean conditions, the reactions are slowed, and the flame envelope may thicken, making the apparent smoke cloud size larger.

Agglomerated Droplets

The first set of data presented for the agglomerates is the overall size of the oxide smoke cloud surrounding the burning droplet as a function of measured agglomerate surface size, as shown in Fig. 10. Again, the smoke cloud size r/r_s is nondimensionalized by the agglomerate surface radius, and each data point (out of the 194 included) represents the average of two halves of one droplet image. The SRM chamber pressures ranged from 5.9 to 21.2 atm. Note that two wavelengths are again represented, and the combined 490- and 560-nm data are curve fit as $r/r_s = \alpha \cdot D_{\text{surf}}^{-\beta}$, where $\alpha = 32 \pm 11$ and $\beta = 0.47 \pm 0.10$, represented by the mean (solid) line and the error (dashed) lines in Fig. 10. The curve fit for the single droplet data presented in Fig. 9 is included on the plot with the agglomerate data for comparison.

Both the single and the agglomerated droplets approximately follow an $r/r_s \sim \alpha \cdot D^{-0.5}$ relation for the overall smoke cloud size. The only difference in the two is simply the leading term coefficient α, which is slightly smaller for agglomerates than for single droplets, but, as evident in Fig. 10, the two curves really lie within each other's data scatter range. Also note that the scatter range for α for both the single and agglomerated droplets is ~34% of their mean values. Additional analysis was conducted that indicates no significant change in $D_{\text{flame}}/D_{\text{surf}}$ over the pressure range studied.

Aluminum Droplet Burning Rate Correlations

Attention to how the flame size vs diameter relation affects the measurement and calculation of the aluminum droplet burning rate

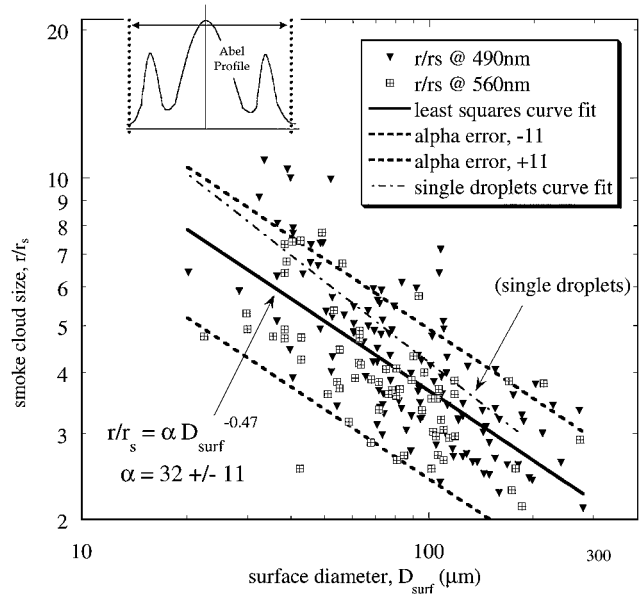

Fig. 10 Nondimensional size of oxide cloud surrounding burning droplet vs droplet diameter for agglomerated droplets burning in SRM flow conditions, $p = 5.9$–21.2 atm; combined 490- and 560-nm data (194 points) are curve fit as $r/r_s = \alpha \cdot D_{\text{surf}}^{-\beta}$, where $\alpha = 32 \pm 11$ and $\beta = 0.47 \pm 0.10$.

laws is important. In our previous work, the D^n burning rate law for single, nonagglomated droplets was measured and calculated for the experimental SRM conditions.[1] The diameter of the outer smoke cloud was measured as a function of time because the 35-mm camera cannot image the interior, that is, the droplet surface diameter. However, to analyze the data, two key assumptions were made, that the droplets each had a 110-μm initial diameter and that apparent r/r_s smoke cloud size was constant throughout the droplet lifetime. With the new data presented here and obtained with the high-speed CCD video and Abel inversion analysis, these two analysis assumptions can be eliminated by correlating the r/r_s vs D_{surf} laws with the burning-rate data.

Before fully describing a data correlation, review of the earlier data analysis for droplet burn time is useful. The analysis derivation is based on the idea of calculating the n power and k slope in the D^n law for burning droplets, presented in Eq. (2). By setting $D = 0$, a burn time t_b can be defined as in Eq. (3):

$$D^n = D_0^n - kt \tag{2}$$

$$t_b \equiv D_0^n / k \tag{3}$$

To calculate n and k, the measured diameter data are curve fit to a power-law equation of the form $y = a \cdot x^b$. Therefore, by using the Eq. (3) definition for t_b, Eq. (2) must be rewritten as Eq. (4):

$$D = \left(D_0^n - kt\right)^{1/n} \qquad \text{or} \qquad D = k^{1/n}(t_b - t)^{1/n} \tag{4}$$

In the form of Eq. (4), the timescale $(t_b - t)$ is treated as time to burnout.

When it is kept in mind that the measured diameters with the 35-mm camera are the outer smoke cloud diameters, and $D_{\text{surf}} = D_{\text{image}}/(r/r_s)$, Eq. (4) must be rewritten as Eq. (6), that is,

$$D_{\text{surf}} = k^{1/n}(t_b - t)^{1/n} \tag{5}$$

$$D_{\text{image}} = (r/r_s)k^{1/n}(t_b - t)^{1/n} \tag{6}$$

In the work reported in Ref. 1, single particles quenched in the chamber were measured to be in the same size range as the loaded aluminum. For each droplet, the smoke size ratio, r/r_s, was then simply calculated by dividing the initial measured diameter by 106 μm. Recall that, there, the critical assumption of the data analysis was that r/r_s remains constant throughout a single droplet burn streak, which we now know is incorrect.

As shown in Figs. 9 and 10, r/r_s can be fit with a power-law curve fit for the dependence on the measured droplet surface diameter:

$$(r/r_s) = \alpha D_{\text{surf}}^{-\beta} \tag{7}$$

Equation (7) is then rewritten in terms of D_{image}, and Eq. (5) is substituted in for D_{surf}, resulting in Eq. (8):

$$D_{\text{image}} = (r/r_s)D_{\text{surf}}, \qquad D_{\text{image}} = \alpha k^{(1-\beta)/n}(t_b - t)^{(1-\beta)/n} \tag{8}$$

By the use of Eq. (8), the original curve-fit parameters a and b calculated in Ref. 1, in the form of $y = a \cdot x^b$, can still be used, but now the D^n law n power and k slope are recalculated as $n = (1 - \beta)/b$ and $k = [a/\alpha]^{1/b} = [a/\alpha]^{n/(1-\beta)}$.

Of course, there has now been another key assumption introduced into this data analysis technique. That is, the r/r_s vs D_{surf} relations used from the Abel data for the correlation represent all droplet diameters equally, regardless of time during droplet burn. For example, the assumption is made that a measured value of r/r_s at $D_{\text{surf}} = 100$ μm represents all droplets at 100 μm, regardless of whether the r/r_s was measured for a newly burning 100-μm droplet, or a 200-μm droplet that has been burning for some time.

The growth of the oxide cap with time would impact this new assumption by tending to shift the r/r_s vs D_{surf} curve down for newly born droplets based on our conclusion that a cap makes the smoke cloud bigger (or the absence of a cap makes the smoke cloud smaller). The shift would chiefly appear at larger values of D_{surf} where most new droplets are born. The analysis would be affected with an underprediction of the initial droplet diameter when calculating the D^n law. The final calculations for burning rate would then be underpredicted for these cases.

Single Droplet Burning Rate Results

The described correlation was performed on the 61 data points presented by Melcher et al.[1] for single droplets burning in SRM conditions for pressures of 13–22 atm. Given a normal distribution, the mean is $n = 0.74$, with a standard deviation ± 0.28. Because the mean is close to 0.75 within the standard deviation, the correct D^n law can be approximated with $n \sim \frac{3}{4}$.

The data are skewed from a Gaussian normal curve, and a gamma distribution was calculated instead. Gamma distributions are typically used in situations where a lower boundary to the data exists,[16] as in this case, where it would be completely illogical for the value of n to be less than zero. The parameters used for the gamma distribution are $\Gamma_1 = 12$ and $\Gamma_2 = 0.063$, valid for the chosen mean of $n = \Gamma_1 \cdot \Gamma_2 = 0.75$ with a standard deviation of $(\Gamma_1 \cdot \Gamma_2^2)^{1/2} = 0.22$.

To calculate a mean k slope, all k for are normalized to a $D^{0.75}$ law. Again, a gamma distribution is fit to the data, and a good distribution shape agreement was found with $\Gamma_1 = 4$ and $\Gamma_2 = 2$, for which the mean $k = 8$ μm$^{3/4}$/ms, with standard deviation $= \pm 4$.

Equation (9) (the final result of the correlation analysis) is the corrected burning-rate law for single droplets in SRM conditions, 13–22 atm, and is plotted in Fig. 11 with the earlier $D^{1.65}$ prediction by Melcher et al.[1] for comparison for a 100-μm-diam single droplet:

$$D^{0.75} = D_0^{0.75} - 8t \tag{9}$$

There are two clear differences in the two curves: the shape and the overall burn time. As shown in Fig. 11, the $D^{0.75}$ law predicts burnout for the 100-μm droplet in ~4 ms, and the $D^{1.65}$ law predicts ~7 ms. The shape of the curve is different because of the correction to the constant r/r_s assumption in the preceding curve analysis. The overall burn time is faster because, in the preceding curve, the initial diameter had to be assumed as 106 μm for all droplets, which is proven a size underestimate according to the Abel data. Therefore, the droplets measured with the 35-mm camera/chopper wheel technique are larger than the expected 106 μm, hinting at slight agglomeration even with the Thiokol 1 propellant.

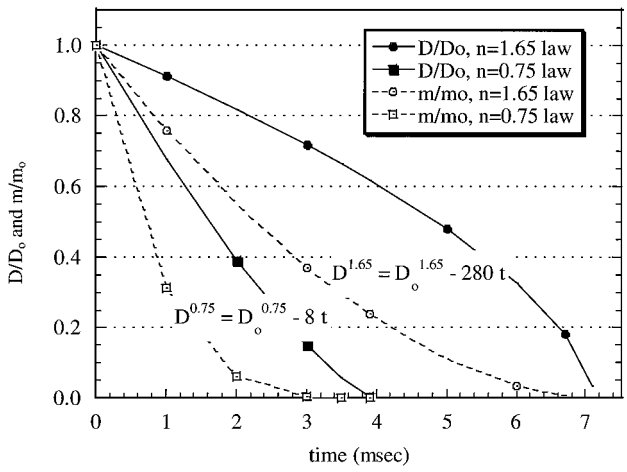

Fig. 11 Comparison of 100-μm single-droplet diameter burn history calculation for mean $D^{0.75}$, $k = 8\ \mu m^{0.75}$/ms law accounting for nonconstant r/r_s smoke size compared with $D^{1.65}$ law previously predicted by Melcher et al.[1]

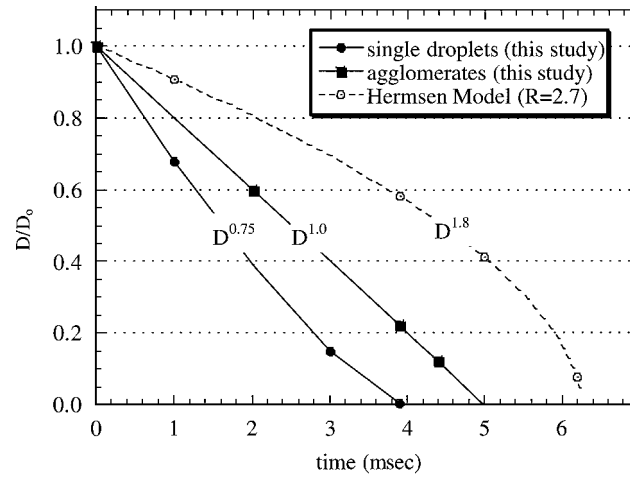

Fig. 12 Comparison of predicted mean burning history of 100-μm droplet for agglomerated droplet data, single droplet data, and Hermsen model.[6]

Because of the difference in curvature of the D^n laws, the mass burning rates, represented by the dashed curves in Fig. 11, are significantly different. In the 100-μm example plotted, the mass/initial mass ratios are calculated using a D^3/D_0^3 approximation, which includes the assumption that relative quality of a droplet would remain constant through its burn history. The mass burns to 10% of its initial value in <2 ms according to the $D^{0.75}$ law, less than half of the burnout time. For the earlier $D^{1.65}$ law, the mass is 10% after ~5 ms, which is about 70% of the burnout time.

It would be useful to consider the effect of pressure on the burning rate law. As described in the Introduction, the burning rate slope k increases as pressure increases. In other words, droplets burn faster when pressure is increased. In Ref. 1, Melcher et al. reported that k increased approximately linearly over the pressure range studied, 13–22 atm in SRM conditions. However, when the data are processed with the new correlation and normalized with the $D^{0.75}$ law, the resulting data exhibit little dependence on pressure within the data scatter. It would be surprising to see a significant effect over the 13–22 atm pressure range studied here, assuming Hermsen's $k \sim p^{0.27}$ law is correct.[6] When a $p^{0.27}$ law is followed, k would only increase 15%, which still falls within our data scatter.

Agglomerate Burning Rate Results

The correlation for droplet smoke cloud size to droplet burning rate described earlier was also performed on agglomerated droplets burning in SRM conditions for pressures 11–20 atm. For the agglomerate correlation, the smoke cloud size law used was $r/r_s = 32 \cdot D_{\text{surf}}^{-0.47}$, as shown in Fig. 10. For the 53 data points and assuming a normal distribution, the mean is $n = 1.0$, with a large standard deviation ± 0.61.

As was the case when examining the single-droplet data, the agglomerate data are apparently shifted away from the normal curve, and a gamma distribution was calculated. Here, the parameters used for the gamma are $\Gamma_1 = 5$ and $\Gamma_2 = 0.15$, valid for the chosen mean of $n = \Gamma_1 \cdot \Gamma_2 = 1.0$ with a standard deviation of $(\Gamma_1 \cdot \Gamma_2^2)^{1/2} = 0.45$.

To calculate a mean k slope, the k for each agglomerate is normalized to a $D^{1.0}$ law. Again, a gamma distribution is fit to the data, and a relation was found, with $\Gamma_1 = 2$ and $\Gamma_2 = 10$, for which the mean $k = 20\ \mu m^{3/4}$/ms, with standard deviation of ± 14.

The result of the correlation analysis is the burning-rate law for agglomerated aluminum droplets in SRM conditions, 11–20 atm, is Eq. (10):

$$D^{1.0} = D_0^{1.0} - 20t \tag{10}$$

Similar to the results for the single droplets, there is no discernable relationship to pressure within the data scatter over the limited pressure range 11–20 atm.

A comparison of the mean $D^{1.0}$ law for the agglomerates, the mean $D^{0.75}$ law for the single droplets, and the Hermsen model[6] are plotted in Fig. 12 for a 100-μm droplet. Recall that the Hermsen relation claims a correction factor of $R_k = 2.7$ for real SRMs and $R_k = 1$ for laboratory experiments and that $R_k = 2.7$ provides a closer comparison to our conditions findings. For the Hermsen model calculated here, conditions were set at $p = 15$ atm and $X_{\text{eff}} = 56\%$.

As shown in Fig. 12, the agglomerated droplet burns about 1 ms slower than the single-droplet predicted burn time, which is a ~25% increase in burn time for the 100-μm droplet case using the mean diameter burning rate laws. Note that the burn time predicted for the two types of droplets might overlap when considering the uncertainty limits reported earlier. The mean prediction for the agglomerate burn time is still about 2 ms faster than the SRM conditions prediction of the Hermsen model.[6] It is predictable that the mean agglomerate curve is closer to the Hermsen model because the Hermsen curve was developed to represent agglomerating propellants.

The agglomerates might burn slower than the single droplets due to their more heterogeneous composition. As was discussed earlier, agglomerates can contain both propellant fuel and oxidizer contaminants from the propellant surface, as well as excess initial oxide shell mass from the agglomeration process. For a given diameter, a single droplet will have more aluminum mass and available aluminum surface area than an agglomerate. Therefore, following the logic of reduced surface area causing decreased burning rate, it is expected for the agglomerates to burn slower.

Furthermore, it was not an objective of this research to categorize the influence of propellant composition on aluminum droplet burning rate. However, one must consider that propellant formulation may affect the droplet burning, particularly in the case of agglomerates, which can entrain propellant surface contaminants during formation.

Summary

Both single and agglomerated aluminum particles were studied in an SRM laboratory-scale test chamber with optical access to the internal flow, at pressures ranging from 6 to 22 atm and at an average temperature of 2300 K. The chamber was pressurized by burning an AP/HTPB propellant, and the burning aluminum droplets were generated by a second, reduced mass, aluminized solid propellant sample.

The high-speed CCD videos of the propellant surface show that agglomerates can have an initial oxide cap that disrupts droplet flame symmetry while still near propellant surface, but flame/smoke cloud symmetry around the burning agglomerates is attained within the first 5–10% of the burn time. Oxide particulates are ejected from the droplet surface.

The agglomeration phenomena observed at 1 atm was very much different than the observations made at the pressurized SRM conditions, where the pocket mainly applies. At 1 atm, 15–20% of agglomerates exploded or fragmented, but in the pressurized SRM flows, no agglomerate explosions were observed for the pressure range of 6–21 atm, due to the differences in agglomerate formation and resulting quality.

The high-speed CCD video was used to image burning single droplets in SRM flow at 1 atm and from 7 to 20 atm, and agglomerates were imaged at 6–21 atm. The key result from the Abel-inverted image intensity profiles of the burning droplets is that relative overall smoke cloud size is not constant with diameter, but instead grows as the droplet shrinks by $\sim D^{-0.5}$ for both single and agglomerated droplets. The smoke cloud size for the agglomerates is slightly less than that for single aluminum droplets. Under SRM conditions, the droplet flame is reaction limited, resulting in changing relative smoke cloud size as the oxide cap reduces surface area and fuel mass flux. This reaction-limited mechanism is in contrast to the diffusion-limited mechanism in 1-atm air conditions.

The 35-mm camera/chopper wheel technique was used to establish burning rate laws for single droplets over a range of 13–22 atm and agglomerates over 11–20 atm. For single droplets burning in SRM conditions, the diameter law is $D^{0.75} = D_0^{0.75} - 8t$, and for agglomerated droplets, $D^{1.0} = D_0^{1.0} - 20t$. For both single and agglomerated droplets, the burning rate k did not change significantly over the pressure range studied.

Acknowledgments

Funding for this work was by way of two separate sources. The first was the University of Illinois at Urbana–Champaign (UIUC) Multidisciplinary University Research Initiative, from the Ballistic Missile Defense Organization through Office of Naval Research Contract N00014-95-1-1339. Judah Goldwasser was the research program director. Funding was also provided through the Center for the Simulation of Advanced Rockets (CSAR) at UIUC, a U.S. Department of Energy (DOE) Accelerated Strategy Computing Initiative center. M. Heath is the CSAR director. The CSAR research program is supported by the DOE through the University of California under Subcontract B341494. Thiokol, Inc., and Alliant Techsystems, Inc., provided the aluminized propellant samples and formulations. Donna Hanson-Parr of China Lake Naval Air Warfare Center provided the appropriate corrections to the Abel inversion equations. We are also indebted to Bob Geisler of Geisler Technologies for providing feedback and technical discussion. Experiments and laboratory work were completed with the assistance of Thomas Hafenrichter and Patricia Cannon, Eric Solverson, Jason Brzozowski, and Shawn Harnish.

References

[1]Melcher, J. C., Burton, R. L., and Krier, H., "Combustion of Aluminum Particles in Solid Rocket Motor Flows," *Solid Propellant Chemistry, Combustion, and Motor Interior Ballistics*, edited by V. Yang, T. B. Brill, and W. Z. Ren, Vol. 185, Progress in Astronautics and Aeronautics, AIAA, Reston, VA, 2000, pp. 723–747.

[2]Melcher, J. C., *Combustion of Single and Agglomerated Aluminum Particles in Solid Rocket Motor Flows*, Ph.D. Dissertation, Dept. of Mechanical and Industrial Engineering, Univ. of Illinois at Urbana–Champaign, Urbana, IL, Aug. 2001.

[3]Price, E. W., and Sigman, R. K., "Combustion of Aluminized Sold Propellants," *Solid Propellant Chemistry, Combustion, and Motor Interior Ballistics,* edited by V. Yang, T. B. Brill, and W. Z. Ren, Vol. 185, Progress in Astronautics and Aeronautics, AIAA, Reston, VA, 2000, pp. 663–687.

[4]Servaites, J., Burton, R. L., Krier, H., and Melcher, J. C., "Aluminum Particle Ignition and Combustion Using a High-Pressure Shock Tube," *Combustion and Flame*, Vol. 125, No. 1/2, 2001, pp. 1040–1054.

[5]Dreizin, E. L., "Experimental Study of Stages in Aluminum Particle Combustion in Air," *Combustion and Flame*, Vol. 105, No. 4, 1996, pp. 541–556.

[6]Hermsen, R. W., "Aluminum Combustion Efficiency in Solid Rocket Motors," AIAA Paper A81-20558, 1981.

[7]Davis, A., "Solid Propellants: The Combustion of Particles of Metal Ingredients," *Combustion and Flame*, Vol. 7, No. 4, 1963, pp. 227–234.

[8]Pokhil, P. F., Belyayev, A. F., Frolov, Y. V., Logachev, V. S., and Korotkov, A. I., "Combustion of Powdered Metal in Active Media," Foreign Technology Div. Rept. FTD-MT-24-551-73, Wright–Patterson Air Force Base AFB, OH, 1972.

[9]Hartman, K. O., "Ignition and Combustion of Aluminum Particles in Propellant Flame Gases," in 8th *JANNAF Combustion Meeting*, Vol. 1, pp. 1–24. Chemical Propulsion Information Agency, 1971.

[10]TEP, Version 1.06c, Software and Engineering Associates, Inc., 1994.

[11]Dasch, C. J., "One-Dimensional Tomography: A Comparison of Abel, Onion-Peeling, and Filtered Backprojection Methods," *Applied Optics*, Vol. 31, No. 8, 1992, pp. 1146–1152.

[12]Gany, A., and Caveny, L. H., "Agglomeration and Ignition Mechanism of Aluminum Particles in Solid Propellants," *Seventeenth Symposium (International) on Combustion*, Combustion Inst., Pittsburgh, PA, 1978, pp. 1453–1461.

[13]Brulard, J., "Contribution to the Study of the Combustion of Aluminum Particles," *La Recherche Aérospatiale*, No. 118, 1967, pp. 25–49.

[14]Micheli, P. L., and Schmidt, W. G., *Behavior of Aluminum in Solid Rocket Motors*, Vol. 2, No. 3, Air Force Rocket Propulsion Lab., Rept. AFRPL-TR-77-29, 1977.

[15]Brewster, M. Q., and Taylor, D. M., "Radiative Properties of Burning Aluminum Droplets," *Combustion and Flame*, Vol. 72, 1988, pp. 287–299.

[16]Mendenhall, W., and Sincich, T., *Statistics for Engineers and the Sciences*, 4th ed., Prentice–Hall, Upper Saddle River, NJ, 1994.